Heliyon 10 (2024) e37051

Contents lists available at ScienceDirect

Heliyon

journal homepage: www.cell.com/heliyon

Research article

A virtual visualization method for improving the manufacturing accuracy based VPP 3D printers

Zhengdong Yu [a,b], Zhenyu Miao [a,b], Zuoyu Liu [a,b], Bohan Yang [a,b], Tongxing Zuo [a,b], Xiangqin Li [c,d], Huan Wang [a,b], Zhenyu Liu [a,b,*]

[a] Changchun Institute of Optics Fine Mechanics and Physics (CIOMP), Chinese Academy of Sciences, Changchun, 130033, China
[b] School of Optoelectronics, University of Chinese Academy of Sciences, Beijing, 100049, China
[c] Beijing University of Technology, Beijing, 100022, China
[d] Shaoguan University, Shaoguan, 512005, China

ARTICLE INFO

Keywords:
Additive manufacturing
Vat photopolymerization
Pixel blending
Mask image projection
Grayscale optimization

ABSTRACT

Compared to traditional vat photopolymerization 3D printing methods, pixel blending technique provides greater freedom in terms of user-defined lighting sources. Based on this technology, scientists have conducted research on 3D printing manufacturing for elastic materials, biologically inert materials, and materials with high transparency, making significant contributions to the fields of portable healthcare and specialty material processing. However, there has been a lack of a universal and simple algorithm to facilitate low-cost printing experiments for researchers not in the 3D printing industry. Here, we propose a mathematical approach based on morphology to simulate the light dose distribution and virtual visualization of parts produced using grayscale mask vat photopolymerization 3D printing technology. Based on this simulation, we develop an auto-correction method inspired by circle packing to modify the grayscale values of projection images, thereby improving the dimensional accuracy of printed devices. This method can significantly improve printing accuracy with just a single parameter adjustment. We conducted experimental validation of this method on a vat photopolymerization printer using common commercial resins, demonstrating its feasibility for printing high precision structures. The parameters utilized in this method are comparatively simpler to acquire compared to conventional techniques for obtaining optical parameters. For researchers in non-vat photopolymerization 3D printing industry, it is relatively user-friendly.

1. Introduction

3D printing technology, a rapidly emerging process of prototyping, has the ability to fabricate complex-structured components promptly from computer-aided design (CAD) models. This innovative technology has been increasingly popularized and extensively implemented across diverse industries over the past few decades [1]. Currently, the most commonly encountered additive manufacturing techniques can be categorized based on the fundamental molding principle, including but not limited to: selective heat sintering (SHS), selective laser sintering (SLS), selective laser melting (SLM) and so on [2]. Such the manufacturing process can

* Corresponding author. Changchun Institute of Optics Fine Mechanics and Physics (CIOMP), Chinese Academy of Sciences, Changchun, 130033, China.
E-mail address: liuzy@ciomp.ac.cn (Z. Liu).

https://doi.org/10.1016/j.heliyon.2024.e37051
Received 16 May 2024; Received in revised form 26 June 2024; Accepted 27 August 2024
Available online 29 August 2024

significantly shorten customization product development cycle [3–5]. It has been ameliorate and expanded the additive manufacturing techniques applications by scientists in the field of high-performance materials [6–8], bioengineering [9–14], microfluidic chip manufacturing [15–20], robotics [21–23], electronic devices [24–27] and computational imaging and machine vision fields [28].

We center our attention on the vat photopolymerization (VPP) approach that is based on digital light processing, which is commonly referred to as VPP-UVM. This method possesses the advantages of high precision, extensive applicability, rapid production speed, low-cost manufacturing, and more [29,30]. Furthermore, the utilization of the proven DLP hardware system from Texas Instruments (Dallas, TX) not only ensures the reliability of the printer, but also simplifies the overall assembly process, resulting in reduced costs. As a result, the DLP 3D printer is more suitable for use as a testing machine for verifying high-precision model conjectures in the laboratory [31].

However, traditional techniques for enhancing printing accuracy are heavily reliant on several costly aspects, including high-quality resin, high-precision dynamic mask generation devices, and shorter wavelength curing light. Additionally, thanks to pixel blending technology that can be applied to VPP-UVM platforms employing grayscale masks, users have greater freedom in customizing the irradiance profile of the output mask at the VPP-UVM platforms [32,33]. Based on this concept, grayscale masked VPP technology utilizing digital micromirror devices (DMDs) or liquid crystal displays (LCD) as dynamic mask generators can pixelate the exposed plane and achieve pixelated light intensity control. Compared to traditional binary exposure methods with fixed light intensity, this technology can display 256 different levels of grayscales from 0 to 255, corresponding to 256 different levels of curing light intensity.

Hence, researchers have the potential to enhance manufacturing accuracy by effectively optimizing the grayscale of projected images using software at the VPP-UVM platforms. This approach offers a viable means of achieving higher printing plane resolution and improved manufacturing quality, all without the need to make any modifications to the existing dynamic mask generator (see Fig. 1). Consequently, the costs associated with achieving these improvements can be significantly reduced.

Previous studies have shown that grayscale control has been exploited by scientists to improve printing accuracy [34]. Specifically, attempting at constitutive modeling of printed materials as a function of grayscale values and process parameters at finite deformations [33,35], presenting a mathematical or physical approach to adjusting voxel compensation parameter [36,37]. While these investigations have indeed yielded high-precision mask correction techniques, their implementation requires the manipulation of specific and intricate parameters related to resin or printing equipment, which results in a significant improvement in print quality. However, it should be noted that achieving fine-tuned adjustments for such methods and enhancing the accuracy of the printer can be laborious for researchers, particularly those who may not specialize in 3D printing, materials science, or testing.

In the process of device fabrication, the curing range of the light-curing 3D printer is intricately linked to the irradiance of the projected ultraviolet (UV) light. Based on the previous study of the intensity of ultraviolet projection using DMD [38]. On the projection plane, the contour map illustrating the intensity distribution of the projected UV spot, corresponding to an individual micro-mirror of the DMD for a single pixel of projection images, demonstrates an almost annular shape (see Fig. 2). Furthermore, attributable to the optical diffraction effect of the projection lens, the irradiance of the projected UV light spot follows a Gaussian distribution. The irradiance within the x-y projection plane $I(x,y)$ can be expressed using Equation (1). The I0 is the peak power intensity, and w0 is the radius at 13.5 % level of the peak intensity.

$$I(x,y) = I_0 e^{\frac{-2\left(x^2+y^2\right)}{{w_0}^2}} \tag{1}$$

In the irradiated area, segments exposed to a light dose surpassing the resin curing threshold will undergo polymerize, whereas those exposed to an equivalent or sub-threshold dose will maintain their original state or remain in a semi-cured condition. However, the acquisition and analysis of irradiance and the other cure related parameters present inherent challenges for individuals lacking expertise in this specialized research domain.

Therefore, we propose a grayscale correction algorithm based on a serious of easily obtainable parameters that predicts the contour boundaries cured during printing by the estimation of light dose algorithm (see Section 2.3) and performs grayscale adjustment of the sliced images based on the predicted boundaries by grayscale correction algorithm (see Section 2.4), resulting in dimensional accuracy enhancements within the printed devices. The flowchart depicting the grayscale correction algorithm is presented in Fig. 3. This method can significantly improve printing accuracy with just a single parameter adjustment. And the acquisition methods for all parameters used have been explained in the article and supplementary materials, with corresponding annotations indicating the location of the supplementary materials when the respective parameters are used in the main body.

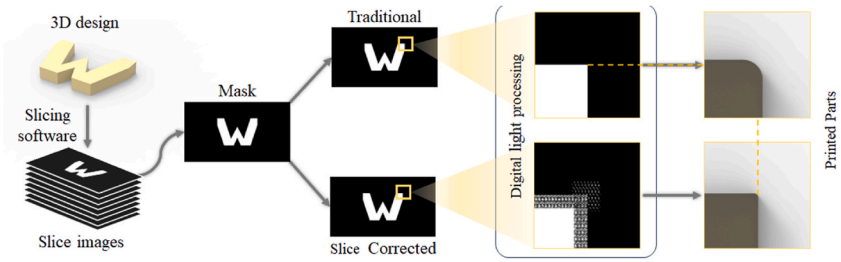

Fig. 1. Schematic representation of the masks correction by computationally processing slice images.

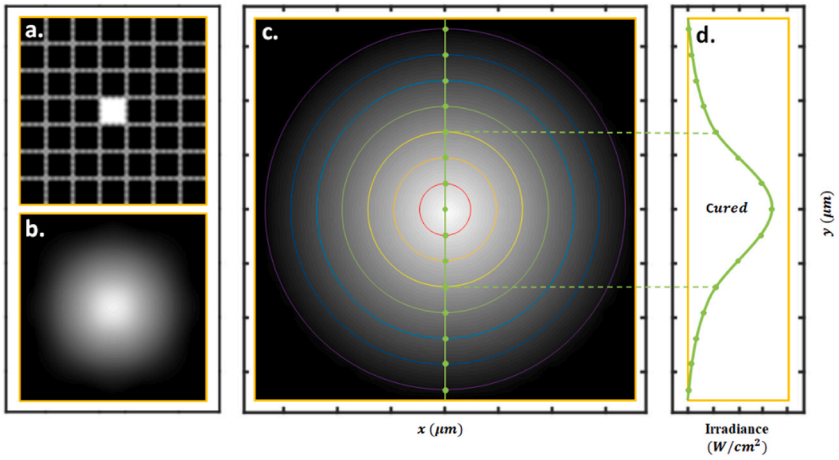

Fig. 2. **a.** The projection image of a single pixel. **b.** The schematic diagram of the UV light distribution. **c.** The distribution of UV dose for an UV spot. **d.** The cross-section plots of modeled Gaussian distribution of UV irradiance along the y-axis.

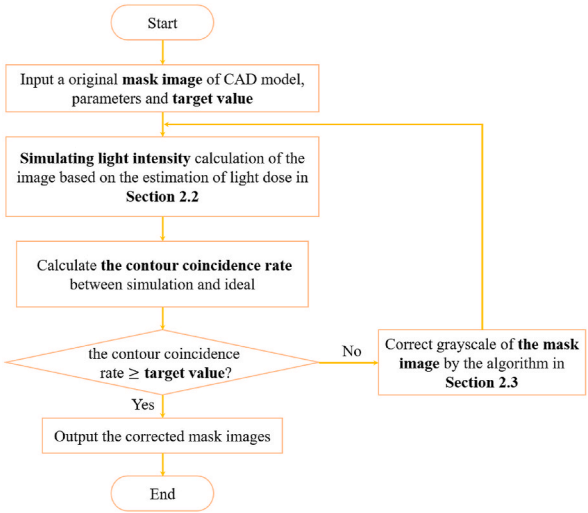

Fig. 3. Flowchart depicting the correction process for mask image.

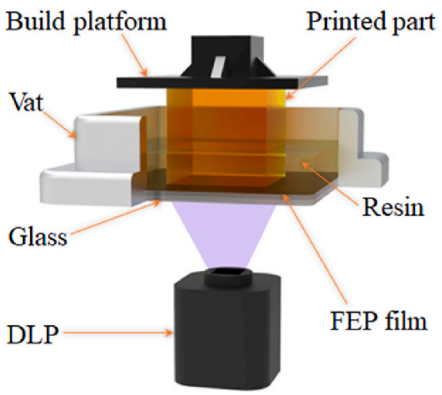

Fig. 4. The detailed structure of the 3D printer.

In addition, a DLP-3D printer validated for mask correction in our previous research [39] was selected for implementation. And we selected a modified resin as the printing material that was simply modified using commercial resin. Furthermore, we conducted single-variable α validation experiments on the key parameters used in the algorithm to demonstrate the superiority of our proposed method.

2. Methods

2.1. 3D printer and materials

We have chosen a conventional assembly DLP-3D printer as our experimental equipment (see Fig. 4). The light source part uses a DLP 4710 DMD purchased from Texas Instruments. The DLP resolution is 1920 × 1080, adjust its size nearly to 20 × 20 μm per pixel on the projection plane. The 385 nm LED light source used has a light intensity of approximately 100–500 mw/cm2. The mask image used by this printer contains a total of 256 grayscale values from 0 to 255, where the white area corresponding to the grayscale value of 255 is the exposure area, and the black area corresponding to the grayscale value of 0 is the non-exposure area. We selected a commercial resin and conducted a simple modified to be compatible with the 3D printer we used. The selected commercial resin for this study is the General-rigidity Resin, which was procured from eSUN. The reagents employed for resin modification are the colouring dye Quinoline Yellow and the dissolving agent 1,6-hexanediol diacrylate (AgiSyn 2816, HDDA) are purchased from MACKLIN. The resin was prepared by this process: First, dissolving 0.1 g of Quinoline Yellow in 5 g of HDDA first, then mixing in the 45 g of commercial resin and sonicated for 15 min.

2.2. The estimation of light dose algorithm

The specific evaluation and virtual visualization process is detailed as follows: Firstly, select a pixel serving as the light source and read its grayscale value g. Subsequently, calculate the range parameter d using Equation (2) based on practical experimental error.

$$d = \alpha \times \frac{L_n}{L_p} \sqrt{\sum_j \left(d_{jreal} - d_j\right)^2} \tag{2}$$

As shown in Fig. 5 a, the range influence parameter d is used to represent the radius of the largest range that a pixel with 255 gray levels of a light source can affect the resin on the projection surface. We can determine the radius of the influence matrix of the light source pixel in the grayscale image through d (see Fig. 5 b). To ensure uniformity of pixel plane light intensity in all directions within the range d (see Fig. 5 c), regulate it based on the distance from the light source pixel. As shown in Fig. 5 d, P_1 is the light source pixel, and P_i is any pixel within the range d affected by this light source pixel. The distance $d_i = \sqrt{(x_2 - x_1)^2 + (y_2 - y_1)^2}$. We estimated the range parameter d through experimental methods, as shown in Fig. 5 e. Select appropriate $d_j = d_1 \sim d_4$ (in this article, d_1 equals to 80 μm, which is four times the resolution size) to print the raised structure based on printer resolution. As shown in Fig. 5 f, choose the layer height Z_{layer} to be 1–3 times the layer height resolution (in this article, Z_{layer} equals to 40 μm which is two times the resolution of layer height). To ensure accurate measurement results, select a $Z_{platform}$ thickness that is not easily deformed (in this article, $Z_{platform}$ equals to 2 mm). The specific model structure is shown in Fig. 5 g. Calculate the range parameter d based on the actual measured

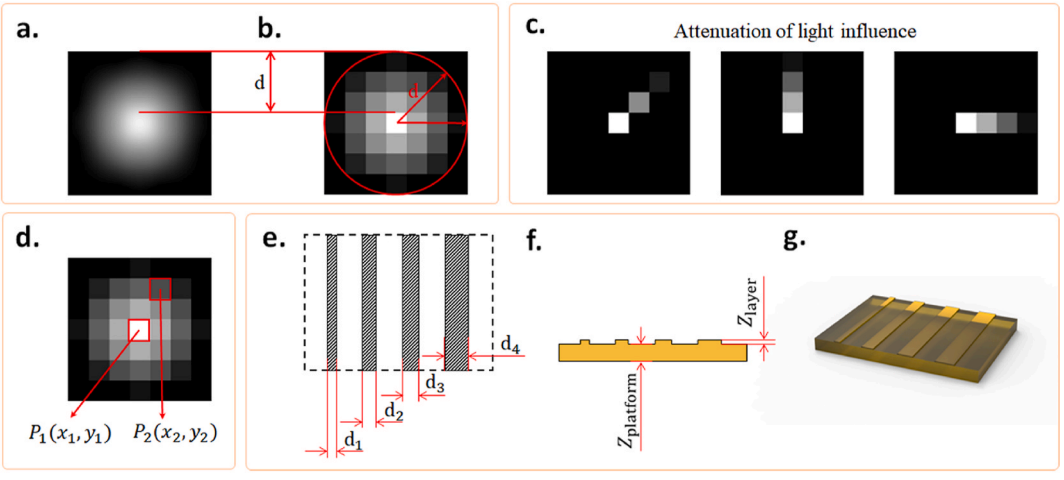

Fig. 5. **a.** Schematic representation of the parameter d. **b.** The application of the d on the slice. **c.** Schematic representation of the attenuation of light influence. **d.** The process of achieve the d_i. **e.** Dimensional diagram of the raised structure. **f.** Dimension diagram of the device thickness. **g.** 3D design of the device printed.

distances $d_{jreal} = d_{1real} \sim d_{4real}$ of the printed model. The ratio L_n/L_p is set to 11/7 for the parameter group used in this article. This parameter L_n and L_p can use the light power of the light source and the threshold of the resin at the curing plane. Use this parameter group only to reduce the trial-and-error period of parameters α. If there is no measurement condition, $L_n = L_p = 1$ can be used, and high printing quality can be achieved by adjusting α alone. In short, here α and L_n/L_p jointly act as adjustment parameters for the influence range. If L_n and L_p cannot be obtained, $\alpha \times L_n/L_p$ can also be set as α in Equation (2).

Thirdly, we introduced the formula for non-uniform numerical dilation (Equation (3)) as the computational substrate for evaluating the mask [40,41]. Select pixels $i(x_i, y_i)$ within a distance range d from the light source pixel $I(x,y)$, calculate the distance d_i from each pixel to the light source pixel. The light intensity distribution at point i, influenced by light source I, is represented as G_i. Assign the grayscale value of each pixel as the rounded G_i.

$$G_i = g \times \left(1 - \frac{d_i}{d + 0.2}\right)^{\beta} \tag{3}$$

To make the distribution of light dose estimation closer to the actual light intensity distribution, we added a light intensity factor $\beta = \omega \times (g/255)^2$ to the grayscale influence formula G_i. Here, the parameter ω is an empirical parameter, which is derived from the intensity decay within the range, used to adjust the amplitude of the intensity of light at the points at different distances from the light source. In this text, the value of ω is 2.1. This process results in an influence matrix of grayscale value g for a single pixel selected as a light source (see Fig. 6 Effect). Fourthly, use the calculated grayscale influence matrix of a single pixel as the basic element and overlay the influence matrix of the selected light source pixel onto the grayscale result image. Finally, matrices of influence for all light source pixels are accumulated based on the characteristics of the light source used.

In this paper, the light source is LED, and the total accumulated light dosage for a certain pixel is calculated as the sum of contributions from each light source pixel within the range of influence. After global calculation, to facilitate evaluation of whether pixel points are cured, normalization processing is applied to all element values to generate the simulated result. The corresponding actual exposure distribution schematic of this simulation result is shown in Fig. 6 Actual Illumination. This novel approach enables us to estimate the accuracy of the mask in terms of its correspondence to actual manufacturing processes.

2.3. Grayscale correction algorithm

Based on the estimation of light dose method proposed in Section 2.2, boundaries can be extracted from the grayscale mask image of light dose distribution. As shown in Fig. 7a and b, we first select a pixel map of the light source. The size of the light source part of the pixel map is greater than or equal to twice the range of the influencing parameter d, ensuring that the grayscale image can calculate the light dose distribution and capture sufficient grayscale values affecting the contour edges. The estimation the light dose of the slice shows in Fig. 7 c. Select the region that can be fully influenced, and use green to represent its ideal contour. Pixels that are a distance of d_c away from the green region are recorded as the quasi-cured contour pixels, and mark this area as blue pixels (see Fig. 7 d). Record the grayscale value of the blue pixels as the boundary element grayscale value, which is also the solidified threshold T_c in the light dose evaluation.

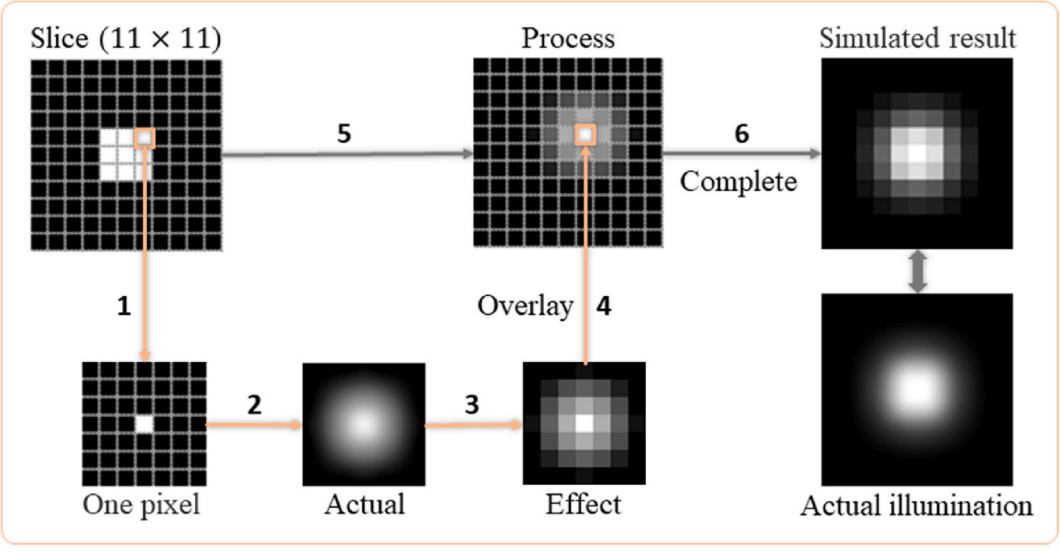

Fig. 6. Schematic representation of the light dose estimation process.

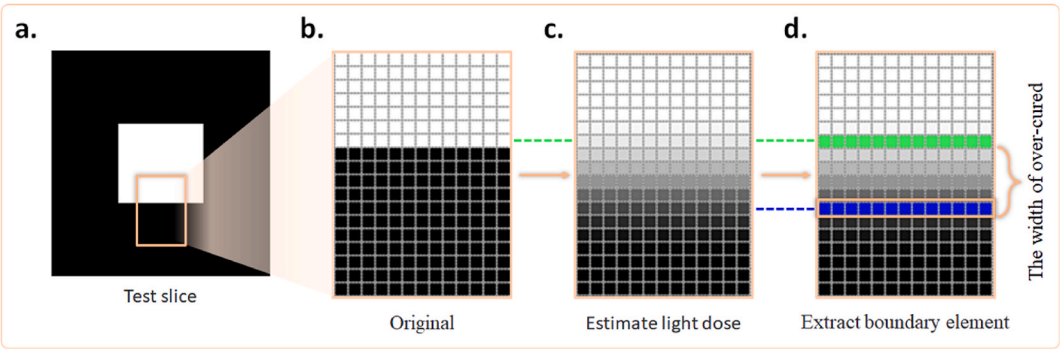

Fig. 7. **a.** Test slice used for extracting grayscale values of contour elements. **b.** Local enlarged view of the slice. **c.** Estimation of light dose. **d.** Extraction of pixels for quasi-cured contour.

$$d_c = \sqrt{\sum_{j=1\sim4} \left(d_{jreal} - d_j\right)^2} \tag{4}$$

Based on the quasi-cured contour extraction mentioned above, as illustrated in Fig. 8, divide the areas into under-cured and over-cured regions. Calculate the difference set between the estimated cured region and the preset cured region. Define the intersection of the difference set with the preset cured region as the under-cured region (see Fig. 8 c), and consider the portion of the difference set that does not intersect with the preset cured region as the over-cured region (see Fig. 8 d).

Consider a single pixel as the source of light. If this pixel's optical influence range d, overlaps with the area that has been over-cured, it will be regarded as an influencing source pixel for the over-cured region. The set of these pixels is referred to as the over-cured influence source region (G). Similarly, the set of light source pixels whose optical influence range d intersects with the under-cured area is defined as the under-cured influence source region (AQ).

We propose the method for correcting over- and under-cured regions that is based on adjusting the gray values of the influence source pixels that affect these regions on the mask. The concept of correcting over-cured regions involves reducing the gray value of over-cured influence source pixels, thereby reducing the overall light dosage received by the affected regions. Conversely, the concept for correcting under-cured regions is to increase the gray value of under-cured influence source pixels that affect the under-cured regions. If the gray value of a light source pixel is already at its maximum, new light source pixels are added within the range that can influence the under-cured region, thereby enhancing the light dosage to the affected region. The procedure described above entails a recurring evaluation of the quasi-cured contours within the sliced grayscale image, accompanied by adjustments to the grayscale levels. These adjustments are made until the convergence of the overlap rate between the ideal contour and the quasi-cured contour meet requirements.

However, because each step of the optimization process adjusts the entire influence source region, it is prone to getting trapped in a

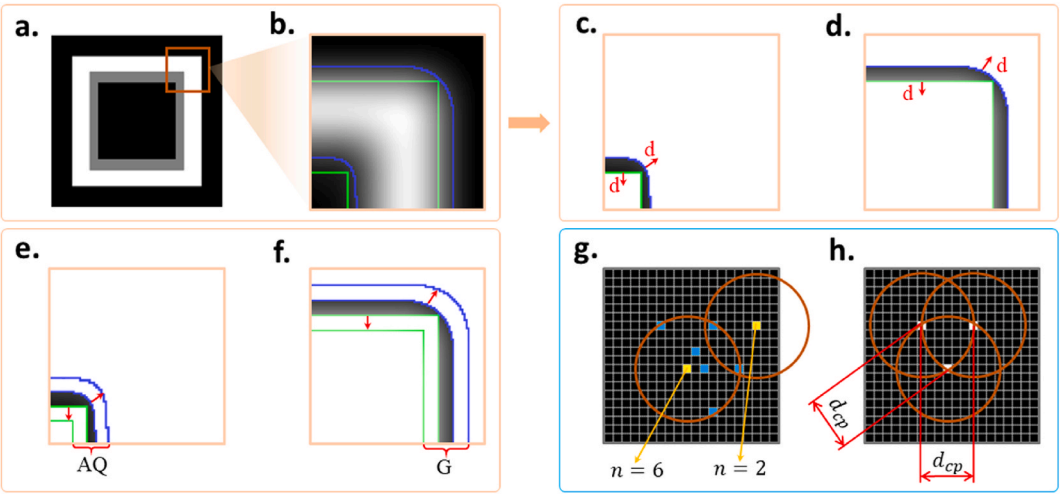

Fig. 8. **a.** To be optimized slice. **b.** Calculate contour information. **c.** Extract the region impacting under-cured pixels. **d.** Extract the region impacting over-cured pixels. **e.** The under-cured influence source region (AQ). **f.** The over-cured influence source region (G). **g.** Calculate the auxiliary parameter n. **h.** Schematic diagram of select point by applying circle packing.

local optimal solution, resulting in subpar optimization results. Therefore, we propose the simple slice optimization method that uses a circle packing-based light source pixel selection method to avoid the correction algorithm from converging to a local optimal solution during iteration.

As Fig. 8 g shows that influence source pixel points within the region (yellow points) are auxiliary parameter based on the number n of over- or under-cured pixel points (blue points) to be processed within their influence range d. The pixel with the largest n within the selected region is taken as the starting point, and the radius d_{cp} of a filling circle is used to extract all centroid elements as the optimized pixel points within the selected region. In a simple term, pixel points that are approximately equidistant are extracted as optimization points. This Points selection method ensures both the uniformity of light source pixel influence during optimization and avoids getting trapped in local optimal solutions to some extent by alternating the selection of adjacent pixel points.

To achieve a lucid exposition of the algorithm's essence, we have chosen a test sample slice image which features both under-cured and over-cured regions for our experimental investigation. The specific process (see Fig. 9) of correct a mask is as follows: Step 1, identify the quasi-cured contour (blue line) and ideal contour (green line) of the slice based on the contour element gray value calculated. Step 2, extract the areas of under-curing and over-curing based on the identified contours. Step 3, perform circle packing to

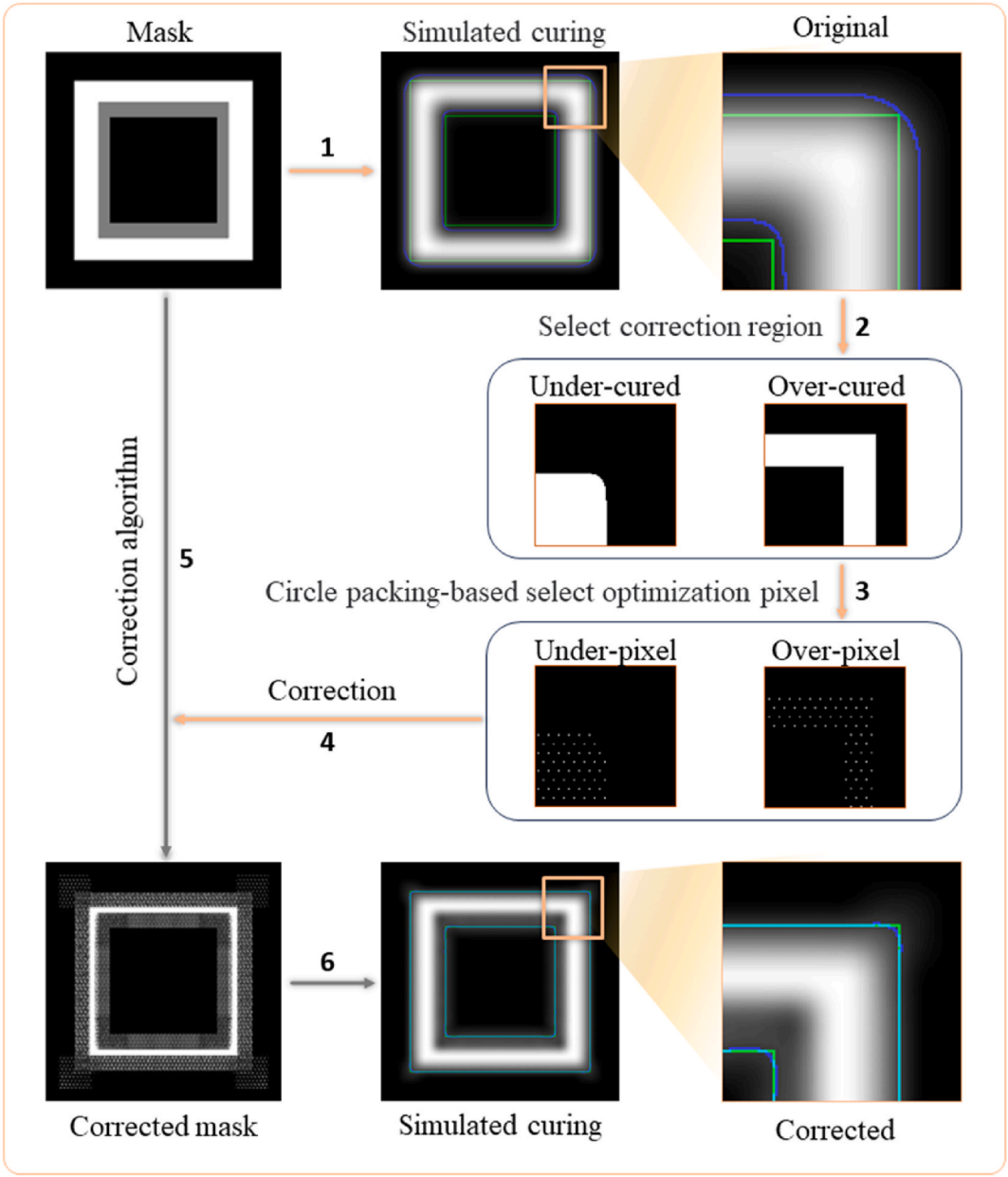

Fig. 9. Schematic representation of one step of the correction algorithm process.

fill the area, and extract the centroid elements of these circle. Step 4, correct the gray value g_u to g_{uc} of the under-pixel corresponding to the slice element using formula (5) based on the characteristics n and n_{max} of the extracted centroid element (the n_{max} represents the maximum value of n obtained in the same calculation step). Correct the gray value g_o to g_{oc} of the over-cured-pixel using formula (6).

$$g_{uc} = g_u - \left\lceil \frac{n \times g_u}{2n_{max}} \right\rceil \tag{5}$$

$$g_{oc} = g_o + \left\lfloor \frac{n \times (255 - g_o)}{2n_{max}} \right\rfloor \tag{6}$$

Finally, we repeat the four steps as an iterative process until the overlap rate between the quasi-cured contour and the ideal contour meets the preset requirements, and export the corrected slice. The quasi-cured contour and ideal contour of the slice are detected (the overlapped part between the quasi-cured contour and the ideal contour is represented by a light blue line). The specific iterative process is shown in Supplementary Fig. 5. In addition, we discussed the optimization pixel selection method and the iterative optimization method in the Supplementary Method, and disclosed their pseudo-codes.

2.4. Optimization algorithm

In order to facilitate a better understanding of the algorithm, the overall optimization process is explained from a mathematical optimization perspective as follows. In Step 1, we select a slice image to be corrected as the grayscale image matrix $\boldsymbol{M}$. We then define the ideal cured region as $\boldsymbol{A}_I$ and record the contour elements of the exposed region as ideal contour elements. Meanwhile, we record the ideal contour elements as $\boldsymbol{L}_I$ (since traditional slicing methods typically define all ideal solid regions as exposed regions). In Step2, we seek to estimate the range of distribution d of the light dosage for a single pixel light source through a series of experiments, and based on this range, we construct a discretized light dosage distribution matrix $\boldsymbol{M}_E$. In Step3, we estimate the overall light dosage distribution matrix $\boldsymbol{M}_V$ of the slice image based on the light dosage distribution matrix $\boldsymbol{M}_E$ of the single pixel light source (Steps 2 to 3 are detailed in Section 2.2). In Step 4, we identify the region where the estimated light dosage is greater than or equal to the threshold T_C as the effective planned solidification region $\boldsymbol{A}_V = (\boldsymbol{M}_V - T_C)^+$. The contour elements of this region are designated as the quasi-cured contour elements, and these planned solidification contour elements are recorded as $\boldsymbol{L}_{VC}$. In Step5, let $\boldsymbol{A}_C = \lceil \boldsymbol{A}_V / max(\boldsymbol{A}_V) \rceil - \lceil \boldsymbol{A}_I / max(\boldsymbol{A}_I) \rceil$ ('$\lceil \boldsymbol{A} \rceil$' represents the ceiling **A**). Define the over-cured region in the non-ideal cured region as $\boldsymbol{A}_{CO} = \boldsymbol{A}_C{}^+$, and the under-cured region as $\boldsymbol{A}_{CU} = \boldsymbol{A}_C{}^-$. In Step6, extend the regions $\boldsymbol{A}_{CO}$ and $\boldsymbol{A}_{CU}$ to cover the entire range that can influenced them, denoted as $\boldsymbol{A}_{COE}$ and $\boldsymbol{A}_{CUE}$. In Step7, Select the pixels P_C within the extended regions $\boldsymbol{A}_{COE}$ and $\boldsymbol{A}_{CUE}$ that are candidates for optimization. Adjust the gray value $\boldsymbol{G}_u$ of P_C based on pixel influencing factors to obtain $\boldsymbol{G}_{uc}$. Repeat Steps 3 to 7 (Steps 4 to 7 are detailed in Section 2.3) within the specified range of influencing parameters $\alpha \in (i, j)$ until the minimum value of $O(\boldsymbol{G}_{uc}) = \|L_I \oplus L_{VC}\|_F$ is obtained, where F represents the Frobenius norm and the "$\oplus$" is the two values involved in the computation yield a result of 0 if the numerical values at the same coordinate position are identical, and 1 otherwise. The iterative optimization problem of the correction algorithm, where the objective is to minimize compliance can be written as:

$$\begin{aligned}
&\boldsymbol{min}: \\
&O(\boldsymbol{G}_{uc}) = \|L_I \oplus L_{VC}\|_F \\
&\boldsymbol{subject\ to}: \\
&\boldsymbol{M}_E \leftarrow d \\
&\boldsymbol{M}_V(x, y) = \sum_{n=0}^{N} D_n(x, y) \subset \boldsymbol{M}_E \\
&\boldsymbol{A}_V = (\boldsymbol{M}_V - T_C)^+ \\
&\boldsymbol{A}_C = \lceil \boldsymbol{A}_V / max(\boldsymbol{A}_V) \rceil - \lceil \boldsymbol{A}_I / max(\boldsymbol{A}_I) \rceil \\
&\boldsymbol{A}_{CO} = \boldsymbol{A}_C{}^+, \boldsymbol{A}_{CU} = \boldsymbol{A}_C{}^- \\
&\boldsymbol{A}_{COE} \leftarrow \boldsymbol{A}_{CO}, \boldsymbol{A}_{CUE} \leftarrow \boldsymbol{A}_{CU} \\
&P_C \leftarrow \boldsymbol{A}_{COE},\ \boldsymbol{A}_{CUE} \\
&0 \le \boldsymbol{G}_{uc}(P_C) \leftarrow \boldsymbol{G}_u(P_C) \le 255 \\
&\alpha > 0
\end{aligned} \tag{7}$$

3. Result and discussion

3.1. Accuracy of linear manufacturing

This section provides an account of the experimental findings obtained through adjusting the key parameters of the proposed approach. Initially, a series of single-variable experiments were conducted to vary the key parameters, and the experimental protocol used therein was described in minute detail, in addition to the examination of its relationship with print quality. Subsequently, the impact of these parameters on the final printed product was analyzed and interpreted. Moreover, the section also highlights the influence of these parameters on the printing process.

We test the uniformity of the printer's light curing influence range by printing and testing the device depicted in Fig. 10 a, which features three surface strip-like structures with different layout directions. To detect pixel influence range in detail, we set three feature widths for each structure, from low to high, namely 100 μm, 200 μm, and 300 μm. Generally, the lowest feature width is set to 4–5 times the effective pixel width according to the comprehensive performance of the printer. Due to two limiting factors: first, for small structures, the exposure dosage required for printing these features is significantly different from that required for large structures, and their non-linear oxygen depletion threshold requires that energy deposition be able to (square) expand feature sizes [42]. Second, small structures are more susceptible to instability conditions (such as optical device defects) than large structures. As Fig. 10 b shows, the over-curing degree of different direction structures is uniform. Therefore, we arbitrarily selected the device with a feature structure

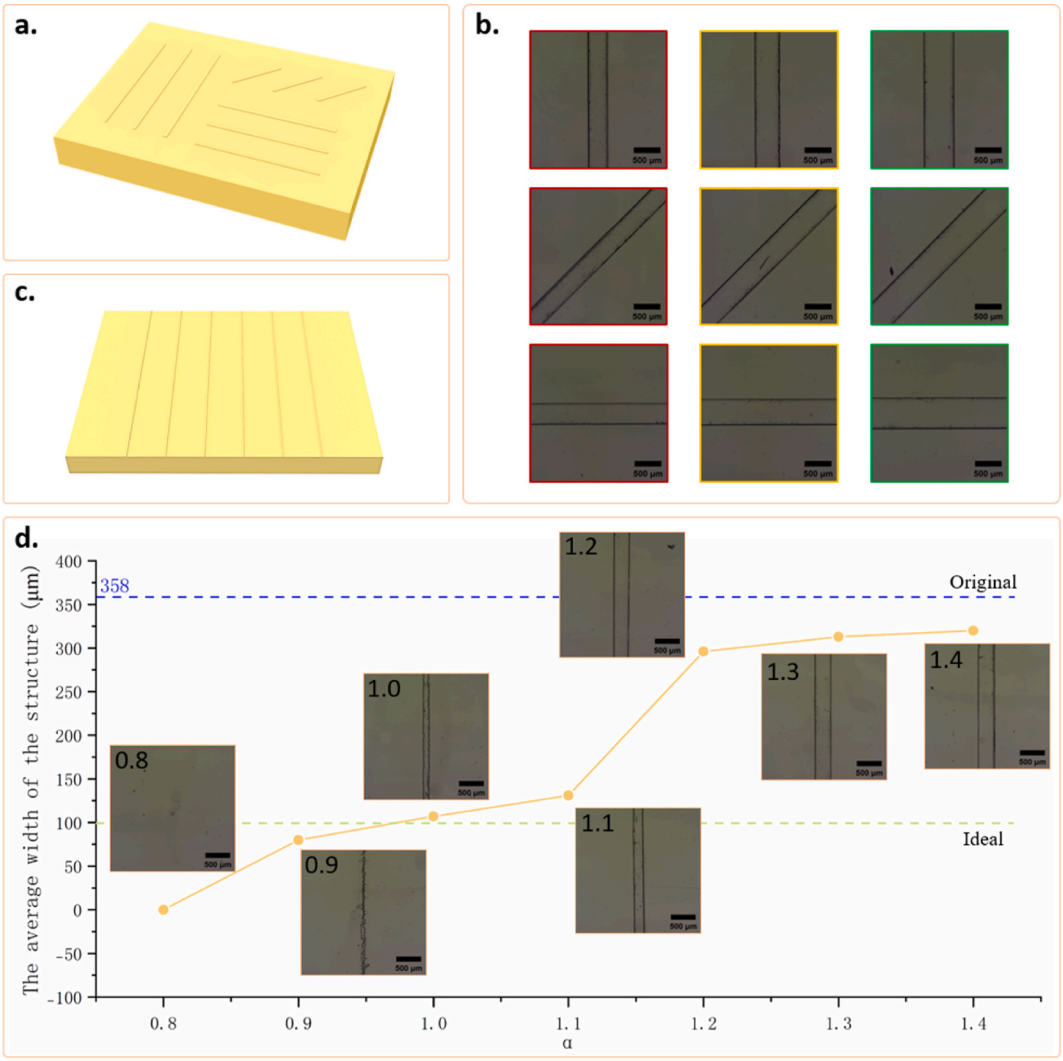

Fig. 10. Critical parameter analysis. **a.** Schematic of the device used to investigate the impact of printing accuracy on uniformity. **b.** Micrographs of the uniformity testing structure, with the red border highlighting the 100 μm feature structure, the yellow border the 200 μm feature structure, and the blue border the 300 μm feature structure. **c.** Schematic of the device used to investigate the parameter α's impact on printing accuracy. **d.** Analysis of alpha's impact on dimensional accuracy.

width of 100 μm (see Fig. 10 c) as the test object to conduct printing quality research with α as the sole variable.

With reference to the printing resolution implemented, we have selected an α array with an interval of 0.1. Each incremental change of α by 0.1 within the studied range corresponds to a corresponding change in the influence range parameter d by one feature pixel width, as graphically represented in Fig. 10 d. This figure presents an analysis chart of the influence of α on printing quality. Before optimization, the average feature size of the printed structure was found to be 358 μm. At the α value of 0.8, the structure was found to be insufficiently cured, leaving behind residual traces that were indistinguishable as to whether they were a part of the manufactured structure. The α value of 1.0 resulted in the feature size of the structure being closest to the ideal size. Furthermore, as the α value increased, the cured range of the printed structure after optimization gradually expanded. It is observable that when the detection equipment is unable to effectively detect the specific parameter enumerated in formula (2), it is possible to adopt the values of L_n and L_p both equal to 1.0, and achieve high printing accuracy solely through the adjustment of α. As Fig. 10 d shows that the dimensional error generated by the machining has been reduced by 96 %.

3.2. Accuracy of angle shapes manufacturing

Due to the potential for boundary quality degradation or irregularities under pixel-based light modulation, we conducted printing quality assessments for the printed structures with sharp-edged contours based on the parameter α selected. As Fig. 11 depicts, we conducted printing quality evaluations on two types of right angles with different orientations relative to the solid region. It can be observed that the use of adjusted α value results in a not smooth boundary contour.

This phenomenon occurs due to the adjustments in grayscale during the optimization process, inherent leading to an uneven state of the pixels in the anticipated solidified corners. Our proposed method does not compromise shape accuracy in its pursuit of enhancing size manufacturing precision. The anomalies depicted in the figure, often misconstrued as inaccuracies stemming from algorithmic errors, actually represent relict structure located within intricate corner regions. These intricacies pose computational and processing challenges, particularly in the shape of special angle regions affected by curing or under-curing. Our proposed algorithm, which relies on readily accessible parameters, aims to minimize the relict structure of the corner shapes while ensuring maximum dimensional accuracy. As depicted in Fig. 12, printing structures with 60-degree or 30-degree acute angles, while the optimization sliced may result in less smooth boundaries compared to pre-optimized prints, nevertheless ensures better dimensional and geometric precision.

3.3. Accuracy of smooth curved shape manufacturing

During the printing preparatory phases, it is imperative to account for the manufacturing impact of contours characterized by specific degrees of curvature. Consequently, we selected three circular structures with varying radii for optimized printing experiments, illustrated in Fig. 13.

The uneven pixelation observed in the sliced images stems from the inherent limitations of STL model pixelization during slicing. As

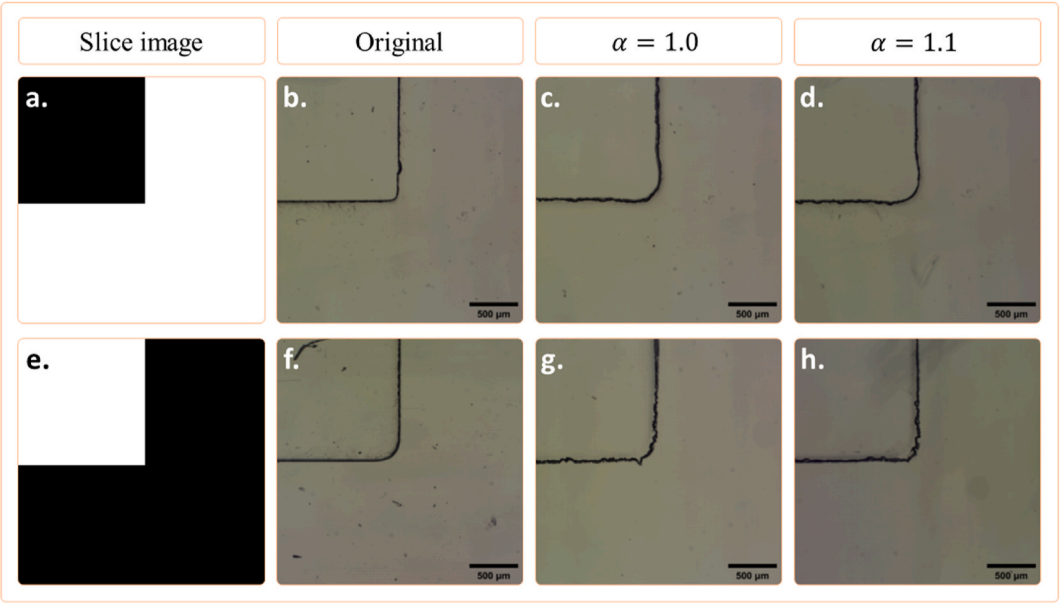

Fig. 11. Feature detail. **a.** The slice image of small angle. **b.** The original state of small angle. **c.** The small angle device printed by the slice of $\alpha = 1$ corrected. **d.** The small angle device printed by the slice of $\alpha = 1.1$ corrected. **e.** The slice image of large angle. **f.** The original state of large angle. **g.** The large angle device printed by the slice of $\alpha = 1$ corrected. **h.** The large angle device printed by the slice of $\alpha = 1.1$ corrected.

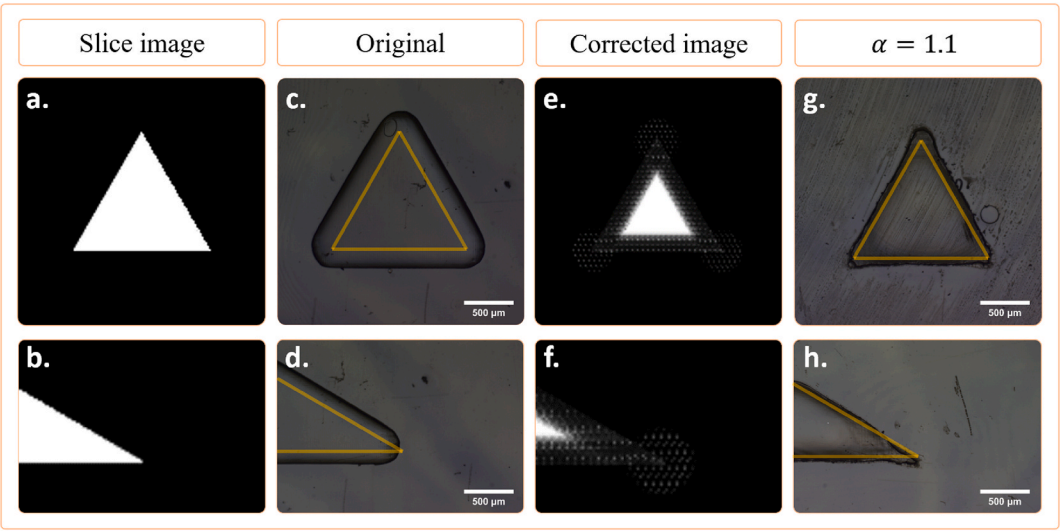

Fig. 12. **a.** A slice image with 60-degree angles structure. **b.** A slice image with 30-degree angle structure. **c. and d.** The original printing structures. **e. and f.** The sliced images after optimized with the algorithm. **g. and h.** Printing structures utilized optimized slice images.

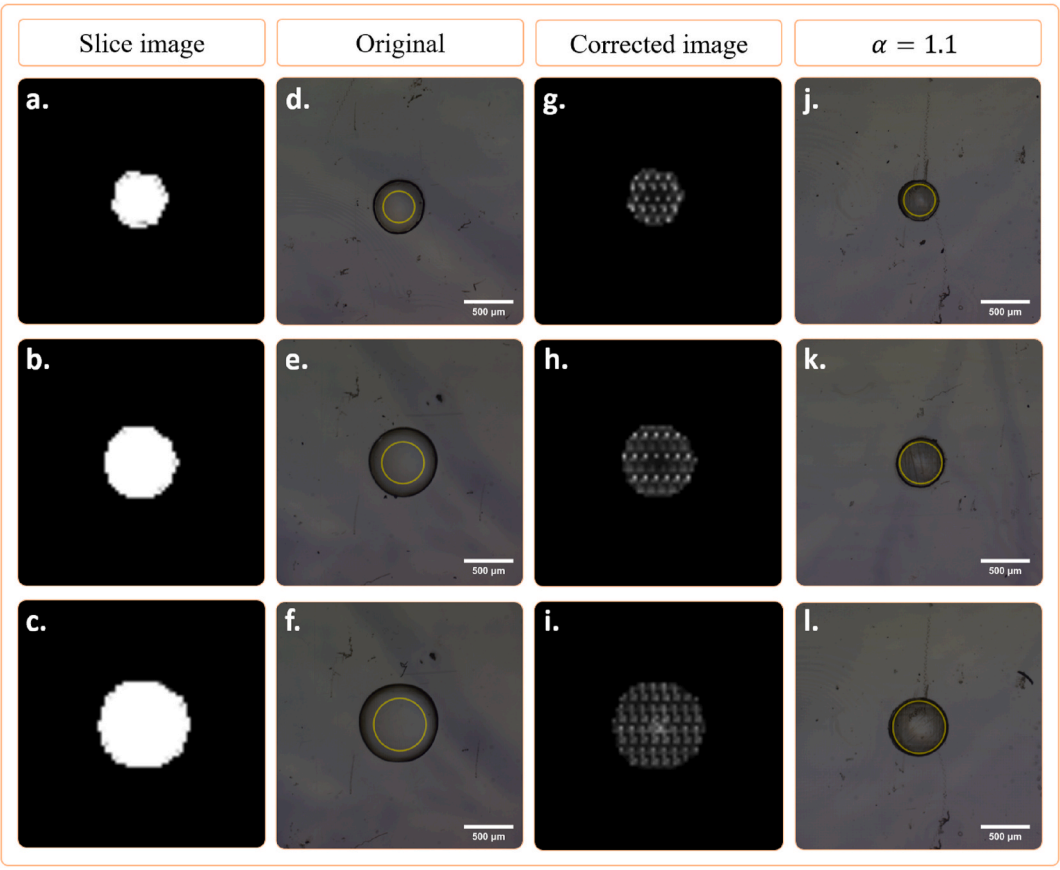

Fig. 13. **a.** A slice image with 300 μm radius circle structure. **b.** A slice image with 400 μm radius circle structure. **c.** A slice image with 500 μm radius circle structure. **d. e. and f.** The original printing structures. **g. h. and i.** The sliced images after optimized with the algorithm. **j. k. and l.** Printing structures utilized optimized slice images.

demonstrated by the outcomes, even for printing boundary structures with significant curvature, this optimization algorithm consistently ensures superior dimensional and shape accuracies.

3.4. Microstructure manufacturing accuracy

The slice correction algorithm based on image blending technology has often been associated with the breakage of the fabricated devices during the printing process. This is because this type of algorithm reduces the light dosage in certain solid areas, resulting in insufficient curing strength of the processed component. Especially for small structures, the exposure dosage required for printing these features is significantly different from that required for large structures. Therefore, to further improvement the functionality of the proposed algorithm, high-resolution microtopographic structures representing complex features in different application fields have been prepared and research (see Fig. 14 a).

As shown in Fig. 14 a, the design of the square topological structure has a wall thickness of 100 μm. Fig. 14 b highlights the scale of this structure, next to which is a Chinese one-corner coin, and the topological structure area is 5 × 5 × 5 mm. The reason for choosing this microstructure lies in the relatively thin solid portion, which, following the aforementioned grayscale optimization only, can easily result in insufficient light exposure in certain microstructures, thus rendering them susceptible to fracture, as Fig. 14 d, e shows. Furthermore, simply increasing the overall exposure intensity would result in excessive part wall thickness or void blockage as shown in Fig. 14 f through normal optimization. Therefore, in addition to normal grayscale adjustments, additional exposure compensation for small structures is required. Fig. 14 c shows the printed structure after microstructure improvement slice correction (Fig. 15 for the slices used). The photo was taken using Huawei Mate 60 pro smartphone.

4. Conclusion

In this paper, we present a method for regulating print accuracy only using several easily obtainable parameters for use with VPP-UVM 3D printing systems, based on image superposition technology. We establish a general light dosage simulation virtual visualization algorithm, the planning algorithm for the points and the grayscale optimization method. We use the proposed algorithm to achieve single parameter variable adjustment to enhance the manufacturing accuracy of VPP-UVM printers. Experimental results show that this algorithm can reliably print within the range of resin curing strength and ensure a certain level of structural integrity. The experiment proves the effectiveness and advantages with single parameter regulation of this method. We have detailed all the parameters used in this algorithm and their simple acquisition methods in this article. In addition, although there is still room for improvement in light dosage estimation and shape accuracy optimization, the proposed method can already be applied to most commercially available VPP-UVM 3D printers, and provide improved high-precision correction methods, providing assist for multi-disciplinary low-cost applications for 3D printing research and development. It is hoped that this can provide help to researchers in non-3D printing industries.

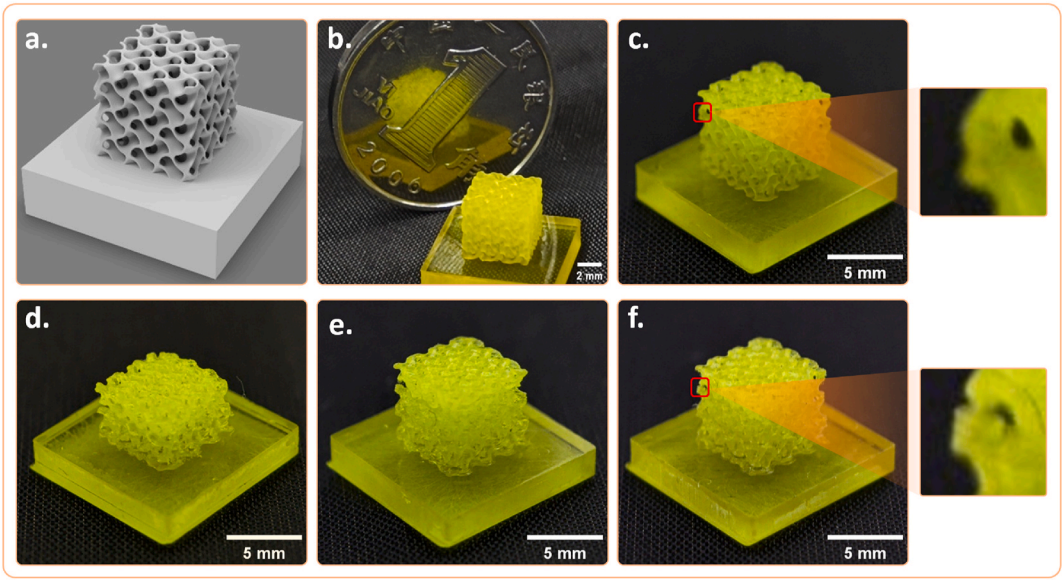

Fig. 14. Examples of printed parts. **a.** 3D design of gyroid lattice structure. **b.** Gyroid lattice next to a Chinese 1 dime coin. **c.** Closeup image of device printed use corrected algorithm. **d. and e.** Insufficient light exposure. **f.** Simply increasing the overall exposure intensity.

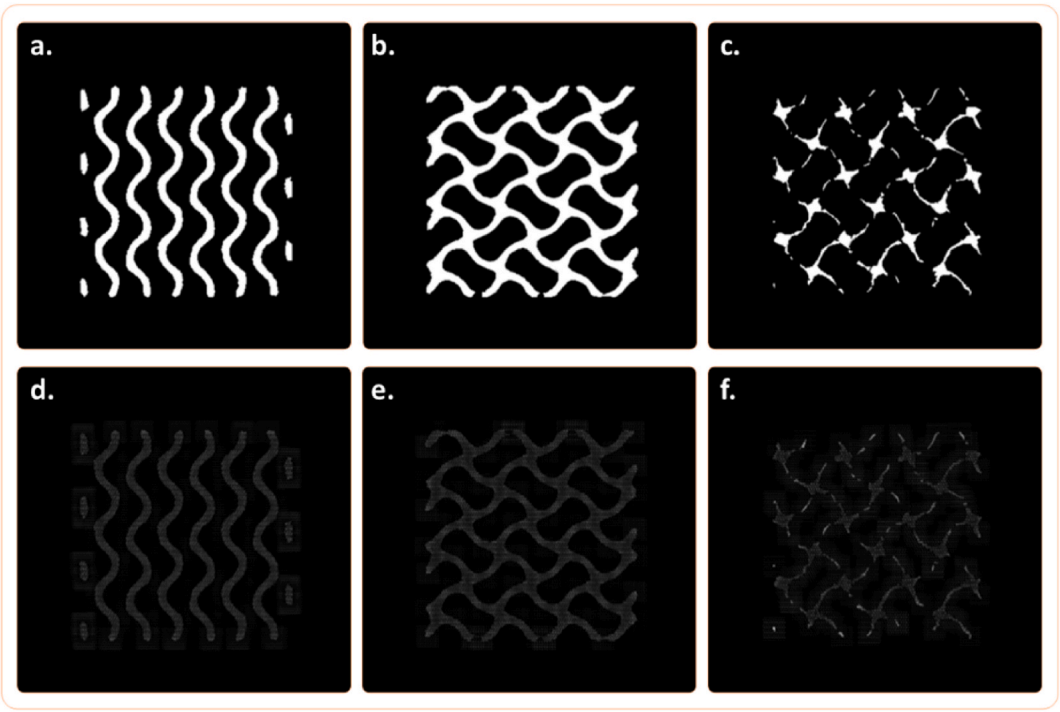

Fig. 15. a. b. and c. Presentation of the test model slices. **d. e. and f.** The sliced images after processing with the algorithm and microstructure improvement.

CRediT authorship contribution statement

Zhengdong Yu: Writing – original draft, Visualization, Validation, Methodology, Investigation, Data curation, Conceptualization. **Zhenyu Miao:** Validation, Methodology, Data curation. **Zuoyu Liu:** Validation, Methodology. **Bohan Yang:** Visualization, Investigation. **Tongxing Zuo:** Validation. **Xiangqin Li:** Investigation. **Huan Wang:** Funding acquisition. **Zhenyu Liu:** Writing – review & editing, Supervision, Conceptualization.

Declaration of competing interest

The authors declare that they have no known competing financial interests or personal relationships that could have appeared to influence the work reported in this paper.

Acknowledgements

The paper is supported by the National Natural Science Foundation of China (62104227).

Appendix A. Supplementary data

Supplementary data to this article can be found online at https://doi.org/10.1016/j.heliyon.2024.e37051.

References

[1] F. Venturi, R. Taylor, Additive manufacturing in the context of repeatability and reliability, J. Mater. Eng. Perform. 32 (2023) 6589–6609, https://doi.org/10.1007/s11665-023-07897-3.
[2] S.A. Adekanye, R.M. Mahamood, E.T. Akinlabi, M.G. Owolabi, Additive manufacturing: the future of manufacturing, Mater. Tehnol. 51 (2017) 709–715, https://doi.org/10.17222/mit.2016.261.
[3] A.P. Zhang, X. Qu, P. Soman, K.C. Hribar, J.W. Lee, S. Chen, S. He, Rapid fabrication of complex 3D extracellular microenvironments by dynamic optical projection stereolithography, Adv. Mater. 24 (2012) 4266–4270, https://doi.org/10.1002/adma.201202024.
[4] J. Warner, P. Soman, W. Zhu, M. Tom, S. Chen, Design and 3D printing of hydrogel scaffolds with fractal geometries, ACS Biomater. Sci. Eng. 2 (2016) 1763–1770, https://doi.org/10.1021/acsbiomaterials.6b00140.

[5] S.-H. Pyo, P. Wang, H.H. Hwang, W. Zhu, J. Warner, S. Chen, Continuous optical 3D printing of green aliphatic polyurethanes, ACS Appl. Mater. Interfaces 9 (2017) 836–844, https://doi.org/10.1021/acsami.6b12500.

[6] X. Zheng, H. Lee, T.H. Weisgraber, M. Shusteff, J. DeOtte, E.B. Duoss, J.D. Kuntz, M.M. Biener, Q. Ge, J.A. Jackson, S.O. Kucheyev, N.X. Fang, C.M. Spadaccini, Ultralight, ultrastiff mechanical metamaterials, Science 344 (2014) 1373–1377, https://doi.org/10.1126/science.1252291.

[7] J.A. Jackson, M.C. Messner, N.A. Dudukovic, W.L. Smith, L. Bekker, B. Moran, A.M. Golobic, A.J. Pascall, E.B. Duoss, K.J. Loh, C.M. Spadaccini, Field responsive mechanical metamaterials, Sci. Adv. 4 (2018) eaau6419, https://doi.org/10.1126/sciadv.aau6419.

[8] J. Borrello, P. Nasser, J.C. Iatridis, K.D. Costa, 3D printing a mechanically-tunable acrylate resin on a commercial DLP-SLA printer, Addit. Manuf. 23 (2018) 374–380, https://doi.org/10.1016/j.addma.2018.08.019.

[9] S.V. Murphy, A. Atala, 3D bioprinting of tissues and organs, Nat. Biotechnol. 32 (2014) 773–785, https://doi.org/10.1038/nbt.2958.

[10] K. Markstedt, A. Mantas, I. Tournier, H. Martínez Ávila, D. Hägg, P. Gatenholm, 3D bioprinting human chondrocytes with nanocellulose–alginate bioink for cartilage tissue engineering applications, Biomacromolecules 16 (2015) 1489–1496, https://doi.org/10.1021/acs.biomac.5b00188.

[11] K. Qiu, Z. Zhao, G. Haghiashtiani, S. Guo, M. He, R. Su, Z. Zhu, D.B. Bhuiyan, P. Murugan, F. Meng, S.H. Park, C. Chu, B.M. Ogle, D.A. Saltzman, B.R. Konety, R. M. Sweet, M.C. McAlpine, 3D printed organ models with physical properties of tissue and integrated sensors, Adv. Mater. Technol. 3 (2018) 1700235, https://doi.org/10.1002/admt.201700235.

[12] S. Mishriki, A.R. Abdel Fattah, T. Kammann, R.P. Sahu, F. Geng, I.K. Puri, Rapid magnetic 3D printing of cellular structures with MCF-7 cell inks, research 2019, 2019, https://doi.org/10.34133/2019/9854593, 2019.

[13] N. He, X. Wang, L. Shi, J. Li, L. Mo, F. Chen, Y. Huang, H. Liu, X. Zhu, W. Zhu, Y. Mao, X. Han, Photoinhibiting via simultaneous photoabsorption and free-radical reaction for high-fidelity light-based bioprinting, Nat. Commun. 14 (2023) 3063, https://doi.org/10.1038/s41467-023-38838-2.

[14] Z. Meng, X. Mu, J. He, J. Zhang, R. Ling, D. Li, Embedding aligned nanofibrous architectures within 3D-printed polycaprolactone scaffolds for directed cellular infiltration and tissue regeneration, Int. J. Extrem. Manuf. 5 (2023) 025001, https://doi.org/10.1088/2631-7990/acbd6c.

[15] C.I. Rogers, K. Qaderi, A.T. Woolley, G.P. Nordin, 3D printed microfluidic devices with integrated valves, Biomicrofluidics 9 (2015) 016501, https://doi.org/10.1063/1.4905840.

[16] A. Urrios, C. Parra-Cabrera, N. Bhattacharjee, A.M. Gonzalez-Suarez, L.G. Rigat-Brugarolas, U. Nallapatti, J. Samitier, C.A. DeForest, F. Posas, J.L. Garcia-Cordero, A. Folch, 3D-printing of transparent bio-microfluidic devices in PEG-DA, Lab Chip 16 (2016) 2287–2294, https://doi.org/10.1039/C6LC00153J.

[17] Y.-S. Lee, N. Bhattacharjee, A. Folch, 3D-printed Quake-style microvalves and micropumps, Lab Chip 18 (2018) 1207–1214, https://doi.org/10.1039/C8LC00001H.

[18] F. Li, N.P. Macdonald, R.M. Guijt, M.C. Breadmore, Increasing the functionalities of 3D printed microchemical devices by single material, multimaterial, and print-pause-print 3D printing, Lab Chip 19 (2019) 35–49, https://doi.org/10.1039/C8LC00826D.

[19] V. Mehta, S.N. Rath, 3D printed microfluidic devices: a review focused on four fundamental manufacturing approaches and implications on the field of healthcare, Bio-Des, Man (Lond.) 4 (2021) 311–343, https://doi.org/10.1007/s42242-020-00112-5.

[20] Y. Xu, F. Qi, H. Mao, S. Li, Y. Zhu, J. Gong, L. Wang, N. Malmstadt, Y. Chen, In-situ transfer vat photopolymerization for transparent microfluidic device fabrication, Nat. Commun. 13 (2022) 918, https://doi.org/10.1038/s41467-022-28579-z.

[21] Y. Kim, H. Yuk, R. Zhao, S.A. Chester, X. Zhao, Printing ferromagnetic domains for untethered fast-transforming soft materials, Nature 558 (2018) 274–279, https://doi.org/10.1038/s41586-018-0185-0.

[22] X. Kuang, K. Chen, C.K. Dunn, J. Wu, V.C.F. Li, H.J. Qi, 3D printing of highly stretchable, shape-memory, and self-healing elastomer toward novel 4D printing, ACS Appl. Mater. Interfaces 10 (2018) 7381–7388, https://doi.org/10.1021/acsami.7b18265.

[23] Z. Zhan, L. Chen, H. Duan, Y. Chen, M. He, Z. Wang, 3D printed ultra-fast photothermal responsive shape memory hydrogel for microrobots, Int. J. Extrem. Manuf. 4 (2022) 015302, https://doi.org/10.1088/2631-7990/ac376b.

[24] D. Espalin, D.W. Muse, E. MacDonald, R.B. Wicker, 3D Printing multifunctionality: structures with electronics, Int. J. Adv. Manuf. Technol. 72 (2014) 963–978, https://doi.org/10.1007/s00170-014-5717-7.

[25] J.A. Lewis, B.Y. Ahn, Three-dimensional printed electronics, Nature 518 (2015) 42–43, https://doi.org/10.1038/518042a.

[26] T. Wei, B.Y. Ahn, J. Grotto, J.A. Lewis, 3D printing of customized Li-ion batteries with thick electrodes, Adv. Mater. 30 (2018) 1703027, https://doi.org/10.1002/adma.201703027.

[27] H. Zhang, X. Zhu, Y. Tai, J. Zhou, H. Li, Z. Li, R. Wang, J. Zhang, Y. Zhang, W. Ge, F. Zhang, L. Sun, G. Zhang, H. Lan, Recent advances in nanofiber-based flexible transparent electrodes, Int. J. Extrem. Manuf. 5 (2023) 032005, https://doi.org/10.1088/2631-7990/acdc66.

[28] B. Bai, Y. Li, Y. Luo, X. Li, E. Çetintaş, M. Jarrahi, A. Ozcan, All-optical image classification through unknown random diffusers using a single-pixel diffractive network, Light Sci. Appl. 12 (2023) 69, https://doi.org/10.1038/s41377-023-01116-3.

[29] G. Comina, A. Suska, D. Filippini, Low cost lab-on-a-chip prototyping with a consumer grade 3D printer, Lab Chip 14 (2014) 2978–2982, https://doi.org/10.1039/C4LC00394B.

[30] M. Layani, X. Wang, S. Magdassi, Novel materials for 3D printing by photopolymerization, Adv. Mater. 30 (2018) 1706344, https://doi.org/10.1002/adma.201706344.

[31] J. Wu, Z. Zhao, C.M. Hamel, X. Mu, X. Kuang, Z. Guo, H.J. Qi, Evolution of material properties during free radical photopolymerization, J. Mech. Phys. Solid. 112 (2018) 25–49, https://doi.org/10.1016/j.jmps.2017.11.018.

[32] V. Singh, B. Hu, K. Toh, S. Bollepalli, S. Wagner, Y. Borodovsky, Making a Trillion Pixels Dance, 2008, p. 69240S, https://doi.org/10.1117/12.773248. San Jose, California, USA.

[33] C. Zhou, Y. Chen, R.A. Waltz, Optimized mask image projection for solid freeform fabrication, J. Manuf. Sci. Eng. 131 (2009), https://doi.org/10.1115/1.4000416.

[34] X. Kuang, J. Wu, K. Chen, Z. Zhao, Z. Ding, F. Hu, D. Fang, H.J. Qi, Grayscale digital light processing 3D printing for highly functionally graded materials, Sci. Adv. 5 (2019) eaav5790, https://doi.org/10.1126/sciadv.aav5790.

[35] I. Valizadeh, A. Al Aboud, E. Dörsam, O. Weeger, Tailoring of functionally graded hyperelastic materials via grayscale mask stereolithography 3D printing, Addit. Manuf. 47 (2021) 102108, https://doi.org/10.1016/j.addma.2021.102108.

[36] Z.D. Pritchard, M.P. de Beer, R.J. Whelan, T.F. Scott, M.A. Burns, Modeling and correcting cure-through in continuous stereolithographic 3D printing, Advanced Materials Technologies 4 (2019) 1900700, https://doi.org/10.1002/admt.201900700.

[37] M. Maennel, L. Selzer, R. Bernhardt, J. Thiele, Optimizing process parameters in commercial micro-stereolithography for forming emulsions and polymer microparticles in nonplanar microfluidic devices, Adv. Mater. Technol. 4 (2019) 1800408, https://doi.org/10.1002/admt.201800408.

[38] Y.-S. Syu, Y.-B. Huang, M.-Z. Jiang, C.-Y. Wu, Y.-C. Lee, Maskless lithography for large area patterning of three-dimensional microstructures with application on a light guiding plate, Opt Express 31 (2023) 12232, https://doi.org/10.1364/OE.482160.

[39] Z. Yu, X. Li, T. Zuo, Q. Wang, H. Wang, Z. Liu, High-accuracy DLP 3D printing of closed microfluidic channels based on a mask option strategy, Int. J. Adv. Manuf. Technol. (2023), https://doi.org/10.1007/s00170-023-11769-4.

[40] O. Sigmund, Morphology-based black and white filters for topology optimization, Struct. Multidiscip. Optim. 33 (2007) 401–424, https://doi.org/10.1007/s00158-006-0087-x.

[41] Y. Guo, H. Pan, E. Wadbro, Z. Liu, Design applicable 3D microfluidic functional units using 2D topology optimization with length scale constraints, Micromachines 11 (2020) 613, https://doi.org/10.3390/mi11060613.

[42] C. Vidler, K. Crozier, D. Collins, Ultra-resolution scalable microprinting, Microsyst Nanoeng 9 (67) (2023), https://doi.org/10.1038/s41378-023-00537-9 s41378-023-00537–9.